Bimodal-Hierarchically Assembled 3-Dimensional $ZnCo_2O_4/NiMoO_4$ Heterostructures Enabling Efficient and Robust Energy Storage Performance

John Hong,[†,‡] *Young-Woo Lee,*[†,‡] *Docheon Ahn,*[⊥] *Sangyeon Pak,*[†] *Juwon Lee,*[†] *A-Rang Jang,*[†,∥] *Sanghyo Lee,*[†] *Bo Hou,*[†] *Yuljae Cho,*[†] *Stephen M. Morris,*[†] *Hyeon Suk Shin,*[∥,*] *SeungNam Cha,*[†] *Jung Inn Sohn,*[†,*] *and Jong Min Kim*[¶]

[†] Department of Engineering Science, University of Oxford, Oxford OX1 3PJ, United Kingdom.

[⊥] Beamline Department, Pohang Accelerator Laboratory, Pohang 37673, Republic of Korea.

[∥] Department of Chemistry, Ulsan National Institute of Science and Technology (UNIST), Ulsan 689-798, Republic of Korea.

[¶] Electrical Engineering Division, Department of Engineering, University of Cambridge, Cambridge CB3 0FA, United Kingdom.

KEYWORDS. hierarchical assembly, heterostructures, porous network structure, ternary transition metal oxides, supercapacitors

ABSTRACT. Designing and tailoring the assembly of complex ternary transition metal oxide (TTMO) structures are a key step in the pursuit of high performance pseudo-capacitive materials for the development of next-generation energy storage devices. Here, we present uniquely assembled 3D heterostructures with hierarchically bimodal morphological features, consisting of a rigidly interconnected primary nanoporous framework of $ZnCo_2O_4$/$NiMoO_4$ core-shell structures and a secondary protruding structure of $NiMoO_4$ layered nanosheets. By benefiting from the combination of the two TTMOs, each with distinct physical characteristics, the assembled 3D $ZnCo_2O_4$/$NiMoO_4$ heterostructures exhibit excellent pseudo-capacitive performance with high capacitances of 6.07 F cm^{-2} and 1480.48 F g^{-1} at 2 mA cm^{-2} as well as an excellent cycling stability of 90.6% over 15000 cycles. Moreover, an asymmetric supercapacitor device can deliver a high energy density of 48.6 Wh kg^{-1}. The superior pseudo-capacitive energy storage characteristics are strongly attributed to the interconnected 3D nanoporous network architecture of the TTMOs along with the secondary layered nanosheets that provide 1) an enlarged surface area, 2) facile and multi-access ion paths, and 3) favorable structural stability. Combined, these results highlight the importance of novel nanostructure design in maximizing the pseudo-capacitive performance and provides a viable way to develop new electrode materials.

1. Introduction.

Pseudo-capacitors, which are an emerging class of electrochemical energy storage system, have been intensively studied over the past few decades in an attempt to address the rapidly increasing global energy requirements whilst also considering the corresponding impact on the economy and the environment.[1-4] The significant importance of pseudo-capacitors as future energy storage devices stems from the fact that, theoretically, they are capable of providing a power delivery and stable cyclability that is superior to that exhibited by Li-ion batteries. In addition, they are also capable of storing a higher energy density than that of electrical double layer capacitors.[5-7] Recent studies have recognized that even though the performance of pseudo-capacitors is essentially determined by the intrinsic physical and chemical properties of the electrode materials, the structural design of the electrode materials can also greatly influence the resulting pseudo-capacitive charge storage behavior as well as the electrochemical kinetics.[8,9] As a result, a tremendous amount of effort has been directed towards the development of carefully structured electrode materials with a controllable size, morphology, stoichiometry, and hierarchical architecture. The aim of this work has been to enlarge the electrochemically active regions to enable faster electrochemical kinetics, which in turn can lead to both higher energy and higher power densities.[10-12]

To date, it has been widely proposed and generally accepted that structural engineering of the electrode materials, through the miniaturization of the size as well as the construction of a porous-structure, is an effective and viable strategy towards steadily improving many transition metal oxides for pseudo-capacitive applications.[13,14] Despite these notable technological advances, it still remains a challenge to tailor complex ternary transition metal oxides (TTMOs), which has the advantage of combining two different mono-component metal oxides into

desirable nanostructured architectures with a maximized surface area, facile and short ion diffusion paths, and a high structural integrity during the charge/discharge process.

Inspired by a basic spinel structural model with 3 dimensional (3D) open channels,[15] in this study, we propose hierarchically assembled 3D heterostructures that comprise a rigidly interconnected nanoporous core-shell network and a secondary protruding nanostructure as illustrated in Figure 1a. Such a proposed electrode design can be expected to enable enhancement of the electrochemical features of the properly selected TTMO electrode beyond the aforementioned requirements for the next generation energy storage devices. Among the various TTMO candidates, $ZnCo_2O_4$ is considered as an ideal backbone material (core) for the robust, porous, and conductive 3D architecture due to the combination of its excellent intrinsic electrical conductivity and its unique cubic spinel crystal structure, which is highly stable and consists of large internal voids as well as 3D internal channels for rapid and multiple access of the ions.[16,17] On the other hand, $NiMoO_4$ is considered to be a potential pseudo-capacitive material for the shell and secondary protruding structure because the excellent redox behavior of the Ni atoms and the good electrical conductivity of the Mo atoms can contribute collectively to yield a high pseudo-capacitive performance.[18,19] Moreover, the open space between the octahedral Ni sites and the tetrahedral Mo sites along with the nanoscale architecture can be particularly beneficial in terms of enhancing the pseudo-capacitive kinetics.

Herein, we report a novel and unique bottom-up synthetic assembly of 3D $ZnCo_2O_4/NiMoO_4$ heterostructures with sponge-like primary nanoporous plates along with a secondary protruding layered nanosheet arrays. The electrodes that are directly integrated onto the 3D microporous current collector provide a unique configuration that consists of a porous and layered network resulting in an enlarged active surface area and multi-access channel. This structure also exhibits

a superior structural integrity that can accommodate any mechanical stress that is induced when cycling through the charge/discharge process, ensuring a favorable electrochemical performance.

2. Results and Discussion

The synthetic process for the hierarchically assembled 3D $ZnCo_2O_4$/$NiMoO_4$ electrode structure is shown in Figure 1b. The $ZnCo_2O_4$/$NiMoO_4$ heterostructures were fabricated using stepwise bottom-up assembly synthesis procedure. Firstly, the nanoporous plate-like structure of $ZnCo_2O_4$ was prepared on a 3D microporous current collector (left of Figure 1b) so as to serve as the rigid backbone structure, which is expected to combine properties of high conductivity, structural stability, and a desirable porous structure (middle of Figure 1b). Then, the resultant nanoporous $ZnCo_2O_4$ plates were uniformly coated by the active nanoscale $NiMoO_4$ shell layers, along with the formation of the layered $NiMoO_4$ nanosheets on the surface of the interconnected core-shell network using a subsequent bottom-up synthesis method (right of Figure 1b). As a result, electrodes with two distinct primary and secondary nanostructures were successfully prepared, enabling rich, rapid, and stable Faradaic redox reactions for pseudo-capacitors.

The hierarchically assembled 3D $ZnCo_2O_4$/$NiMoO_4$ heterostructures were assessed by scanning electron microscopy (SEM), transmission electron microscopy (TEM), and high-angle annular dark-field scanning TEM (HAADF-STEM) measurements. It can be seen that very thin nanostructured $ZnCo_2O_4$ plates with uniform and smooth surface morphology are dispersed across the entire 3D microporous current collector (Figure 2a and S1a-b). TEM studies reveal that the plates are composed of the rigidly interconnected nanoscale grains and pores with a size of 10–20 nm, as shown in Figure 2b and S1c. Moreover, Figure 2c presents the HAADF-STEM image of $ZnCo_2O_4$, further demonstrating the existence of the highly-entangled grains (white

space) and pore channels (black space). The elemental distribution of the $ZnCo_2O_4$ plates is also clearly identified by the energy dispersive X-ray spectroscopy (EDX) mapping analysis (Figure 2d), confirming that the Zn, Co, and O elements are uniformly dispersed on the nanoporous plates.

After a hierarchical bottom-up assembly process to develop the 3D $ZnCo_2O_4/NiMoO_4$ heterostructures, there is an obvious change in the surface morphology of the electrodes with the addition of the secondary nanosheet arrays that protrude from the backbone plate structure, as shown in Figure 2e and S2a-b. Notably, STEM and HAADF-STEM images show morphologically distinct regions, including a primary plate region with an interconnected porous network (the center region in Figure 2f-g and S2c-e, see more detailed information in SI) and the secondary nanosheet region (the edge region in Figure 2f-g). Furthermore, the EDX mapping images taken from the area in the HAADF-STEM image of Figure 2g and inset of Figure S2e show that all the elements (Zn, Co, Ni, and Mo) are uniformly distributed along the hierarchical nanostructures (Figure 2h and S2f). Therefore, these results indicate the formation of $ZnCo_2O_4/NiMoO_4$ heterostructures with additional secondary nanostructures.

To further investigate the detailed structural features of the hierarchically assembled 3D $ZnCo_2O_4/NiMoO_4$ heterostructures, a high-resolution HAADF-STEM image was recorded from the center region of the sample as shown in Figure 3a. The corresponding EDX mapping images show the clear coexistence of all four metal elements on the whole area of the sample (Figure 3b). Interestingly, the EDX signals of the Ni and Mo atom were detected with relatively high intensity on the white dotted area. These findings are believed to be strongly associated with the formation of the secondary $NiMoO_4$ nanosheets on the surface of the $ZnCo_2O_4$ plates. Moreover, Figure 3c-d show atomic scale structural characterization of the $ZnCo_2O_4/NiMoO_4$

heterostructures further investigated by the high-resolution TEM images and the corresponding fast Fourier transform diffraction (FFT) patterns from the region outlined by a yellow dotted rectangle as shown in Figure 3a. These TEM and FFT results clearly reveal two distinct regions in the $ZnCo_2O_4$/$NiMoO_4$ heterostructures: (1) the region 1 is found to be a primary heterostructure region consisting of the active $NiMoO_4$ shell and rigid $ZnCo_2O_4$ core structures, which are determined by three different adjacent lattice spacings of about 0.238, 0.145, and 0.210 nm, which correspond to a (311) plane of spinel $ZnCo_2O_4$, and (600) and (330) planes of monoclinic $NiMoO_4$, respectively;[20, 21] (2) the region 2 is identified as the secondary structure region associated with the layered $NiMoO_4$ nanosheet structure from the observation of lattice fringes with only 0.215 nm spacing, indicating the (400) planes of monoclinic $NiMoO_4$.[21] In addition, the cross sectional HAADF-STEM (Figure 3e-f and S3a) and EDX mapping (Figure S3b) images of the $ZnCo_2O_4$/$NiMoO_4$ heterostructures prepared using a focused ion beam also clearly verify the hierarchical formation of secondary protruding layered nanosheets on the primary nanoporous plates.

Synchrotron X-ray diffraction (XRD) and X-ray photoelectron spectroscopy (XPS) analysis was also performed to further verify the crystal and chemical structures of the hierarchically assembled 3D $ZnCo_2O_4$/$NiMoO_4$ heterostructures. As shown in Figure S4 (see more detailed information in SI), all the reflections in the XRD patterns are unambiguously assigned to spinel $ZnCo_2O_4$ (JCPDS 23-1390) and monoclinic $NiMoO_4$ (JCPDS 86-0361).[22,23] Moreover, Figure 3g shows high-resolution XPS spectra of the Zn 2p, Co 2p, Ni 2p and Mo 3d peak regions with the fitted peak components, clearly revealing the presence of the corresponding metallic elements. This is in good agreement with the EDX results as shown in Figure 2h and 3b. The peak fitting analysis of all the XPS spectra suggests that there exist the compositions of Zn^{2+} and Co^{3+} in the

$ZnCo_2O_4$ structure, and the Ni and Mo exist as Ni^{2+} and Mo^{6+} states, respectively, in the $NiMoO_4$ structure.[24,25] Thus, a comparison of the SEM, TEM, EDX, XRD, and XPS results provides direct evidence that the 3D assembled $ZnCo_2O_4/NiMoO_4$ heterostructures consist of the primary $ZnCo_2O_4/NiMoO_4$ plates and the secondary layered $NiMoO_4$ nanosheet arrays.

On the basis of the obtained heterostructures and chemical composition information, we have evaluated the pseudo-capacitive characteristics of the hierarchically assembled 3D $ZnCo_2O_4/NiMoO_4$ heterostructures. Figure 4 depicts the overall electrochemical performance of the bare $ZnCo_2O_4$ electrode without any additional $NiMoO_4$ layer (denoted as single-TTMO) and the $ZnCo_2O_4/NiMoO_4$ heterostructured electrode with hierarchically bimodal geometrical structures (denoted as bimodal-TTMO). As shown in Figure 4a, a cyclic voltammetry (CV) curve of the bimodal-TTMO exhibits the typical Faradaic redox behavior with a potential window ranging from 0.0 to 0.6 V at a scan rate of 5 mV s^{-1}. The integrated CV area for the bimodal-TTMO sample is much larger than that of the single-TTMO. This indicates that the bimodal-TTMO possesses a superior electrochemical capacitance due to the unique hierarchical core-shell nanostructures with a relatively high surface area, which is consistent with the Brunauer-Emmett-Teller (BET) surface area measurement results (Figure S5). Moreover, all CV curves have similar shapes within scan rates of 5–50 mV s^{-1}, indicating reversible Faradaic reaction behavior (Figure S6a). Further, we plotted the cathodic and anodic current densities as a function of the scan rates from the CV curves of the bimodal-TTMO and have clearly observed a linear relationship with the oxidation reaction (R^2 = 0.99959) and reduction reaction (R^2 = 0.99886) values (Figure S6b). These high values of R^2, close to 1, also imply that our bimodal-TTMO electrode exhibits good reversible redox reaction behavior.[26]

Figure 4b presents galvanostatic charge/discharge (GCD) curves of the bimodal-TTMO at different current densities. Similar to the CV results, the bimodal-TTMO electrode shows typical charge/discharge curves with superior Faradaic redox reaction performance compared to the single-TTMO electrode as shown in Figure S7a. As expected, the area and mass capacitance of the bimodal-TTMO are significantly enhanced to reach 6.07 F cm^{-2} and 1480.48 F g^{-1}, respectively, at a current density of 2 mA cm^{-2} (Figure 4c), which are 4 times more than that of the specific capacitance of the single-TTMO (Figure S7b). Moreover, even at a high current density of 50 mA cm^{-2}, the bimodal-TTMO electrode can achieve a capacitance of up to 959.04 F g^{-1} even at a high current density of 50 mA cm^{-2}.

In addition to demonstrating the substantive electrochemical capacitive performance, we also conducted electrochemical cycling tests to evaluate the capacitance retention capability and structural stability of the electrode. Obviously, it can be seen that the electrode remarkably retains more than 96.8% of its initial capacitance after 3000 cycles at 50 mV s^{-1} (Figure 4d), which shows a superior capacitance retention compared to other reported ternary transition metal oxide electrodes, as summarized in Table S1. It should be noted that under harsh conditions, the bimodal-TTMO exhibits excellent electrochemical cyclability with a capacitance retention of 90.6% after 15000 cycles at a high scan rate of 100 mV s^{-1} (Figure 4e). Inset images of Figure 4e present Nyquist plots (left) and Bode phase plots (right) of the bimodal-TTMO electrode obtained using electrochemical impedance spectroscopy (EIS) measurements to analyze the electrochemical kinetics and stability of the electrode before and after the charge/discharge cycling test. It can be clearly seen that in the Nyquist plots, even after 15000 cycles, semicircles at the high frequency region and straight lines at the low frequency region, which indicate the charge transfer resistance (R_{ct}) and the Warburg impedance (W) associated with ion diffusion

processes, respectively, almost remain unchanged. Moreover, it is also observed that in the Bode plot, the phase angle at low frequency can be maintained at about ~ -77° (the degree for ideal capacitor behavior is close to -90°)[27] over the long-term cycling test. These EIS results indicate that the bimodal-TTMO electrode has superior electrochemical kinetics and stability and hence retains its excellent capacitive behavior during the charge/discharge processes. Additionally, we further analyzed morphological changes of the electrode to investigate the structural stability after long-term cycling testing using SEM examinations as shown in Figure S8. It is revealed that the morphology and the structure of the hierarchical 3D $ZnCo_2O_4/NiMoO_4$ heterostructured electrode remain intact after 15000 cycling tests, demonstrating its structural robustness.

From the point of view of electrode design and material properties, our uniquely designed electrode has multiple distinct advantages that enable superior electrochemical performance, as illustrated in Figure 4f. The first is the hierarchically assembled 3D heterostructures with open interconnected porous channels, providing enhanced surface area and multi-access diffusion pathways for facile and rapid ion transport. The second advantage is the formation of the secondary protruding $NiMoO_4$ nanosheets on the surface of the primary nanoplates, which provide an additional contribution to the improvement of the specific capacitance and electrochemical kinetics because of the high pseudo-capacitive activity combined with the unique layered, open structure that facilitates favorable ion diffusion and adsorption. An additional advantage of our electrode design is that the direct integration of the $ZnCo_2O_4$ backbone structure, which has high electric conductivity and good structural stability, onto the 3D microporous current collector framework ensures fast electron transport and good structural integrity (Figure S6c, see more detailed information in SI), but also stimulates more surface area of the $NiMoO_4$ to become electrochemically active.

To further evaluate the bimodal-TTMO electrode for practical applications, we fabricated an asymmetric supercapacitor (ASC) coin cell with activated carbon (AC) as the anode and the bimodal-TTMO as the cathode. From CV curves of the AC and bimodal-TTMO electrodes (Figure S9a), we have calculated the mass of the AC anode to fulfill the charge balance with the bimodal-TTMO cathode and estimated that the AC//bimodal-TTMO ASC can be operated in a wide potential range from 0 to 1.6 V.[28] Figure S9b presents the CV curves collected at different operating voltage windows at a scan rate of 50 mV s^{-1}, showing capacitance contribution from both the AC anode and the bimodal-TTMO cathode. The inset of Figure S9c depicts typical GCD curves of the ASC at current densities from 20 to 2 mA cm^{-2} within a potential range of 0 to 1.6 V. Accordingly, the maximum specific capacitance of the ASC reaches 136.6 F g^{-1} at a current density of 2 mA cm^{-2} (Figure S9c).

On the basis of the GCD curves, the specific energy density and power density of the ASC were calculated. Figure 5a presents the Ragone plot of the AC//bimodal-TTMOs ASC for the purposes of comparison with other devices reported recently. The ASC device exhibits a high energy density of 48.6 Wh kg^{-1} and also reaches a reasonable power density ranging from 112.7 to 2820 W kg^{-1}. The practical electrochemical performance of our ASC are much higher than those of other reported devices and commercial energy storage devices.[29-37] Moreover, the ASC exhibits excellent cycle life with a capacitance retention of 94.0% after 3000 cycles at a scan rate of 50 mV s^{-1} (Figure 5b). These findings suggest that our ASC device can be used as a promising energy storage system with reliable long-term operation durability. Additionally, we have demonstrated that our optimized three ASC coin cells connected in series can successfully power up to 29 red light-emitting diodes (LEDs) which were assembled in parallel (Inset of Figure 5b and Figure S10).

3. Conclusions

In summary, we have reported hierarchically assembled 3D heterostructures of two different TTMOs to emphasize the importance of designing nanoarchitectures that optimize the intrinsic electrochemical properties and provide a morphology that exhibits a high structural integrity. Such a novel electrode design confirms the significance of the hierarchical nanostructures and the realization of the bimodal-TTMOs as a pseudo-capacitive cathode electrode. Importantly, the synergistic effects of bimodal-TTMOs within their unique interconnected nanoporous network structure, combining with an enlarged contact area, plausible electrochemical kinetics in ion/charge transport and great mechanical stability have been reported, exhibiting a high specific capacitance and a superior long-term cyclability over 15000 charge/discharge cycles. Moreover, the asymmetric coin cell supercapacitor can deliver a high energy density of 48.6 Wh kg^{-1} and a high power density of 2820 W kg^{-1}. Further, it is expected that our approach for rationally designing and tailoring the hierarchical bimodal-TTMO electrode has great potential for energy storage technologies and also contributes to many other application areas dealing with electrochemical processes and ion/charge transport kinetics within nanoporous network structures.

4. Experimental Section

Synthesis of hierarchically nanostructured $ZnCo_2O_4/NiMoO_4$ heterostructures. All the chemicals were of analytical grade and directly used after purchase without further purification steps. Hierarchically assembled 3D $ZnCo_2O_4/NiMoO_4$ heterostructures on a Ni foam were synthesized by a two-step hydrothermal synthetic process. Prior to the hydrothermal synthesis,

the conductive Ni foam was cleaned by sonification using 1.0 M HCl, ethanol, and deionized water. For the synthesis of the $ZnCo_2O_4$ core backbone material, 1.0 mmol of $Zn(NO_3)_2 \cdot 6H_2O$, 2.0 mmol of $Co(NO_3)_2 \cdot 6H_2O$ and 5.0 mmol of urea were dissolved in deionized water to form a clear red solution. The red solution and the cleaned Ni foam were then transferred into a Teflon-lined stainless steel autoclave and kept at 130 ^oC for 5 h. After cooling down, the Ni foam sample was rinsed several times to remove impurities and dried at 60 ^oC for 12 h. In order to obtain the crystallized nanoporous $ZnCo_2O_4$, the Ni foam sample was annealed at 350 ^oC for 2 h with a heating rate of 1 °C min^{-1} under Ar environment. Then, to obtain hierarchically assembled 3D $ZnCo_2O_4/NiMoO_4$ heterostructures, precursors for $NiMoO_4$ were prepared. For this, 1.0 mmol of $Ni(NO_3)_2 \cdot 6H_2O$ and 1.0 mmol of Na_2MoO_4 were dissolved in a mixture solution (deionized water and ethanol) to form a clear green solution. The green solution and the annealed Ni foam sample with a nanoporous $ZnCo_2O_4$ core were transferred into the Teflon-lined stainless steel autoclave and kept at 140 ^oC for 4 h. Finally, after the same cooling and rinsing steps, the Ni foam sample was annealed at 350 ^oC for 2 h under the same heating rate and environmental conditions.

Electrochemical Characterization. The electrochemical performance of the obtained electrodes was tested in a three-electrode configuration consisting of the sample as the working electrode, a Pt mesh as the counter electrode, and a saturated Ag/AgCl electrode as the reference electrode. CV (within the range of 0.0–0.6 V), GCD (within the range of 0.0–0.5 V), and EIS (in the range of 10^{-2} to 10^5 Hz) examinations were conducted using a potentiostat analysis system (PGSTAT302N, Metrohm Autolab). The specific areal and mass capacitance can be calculated according to the following Equation 1:

$$C_A = \frac{I_d * t}{\Delta V * A}, C_m = \frac{I_d * t}{\Delta V * m} \quad (1)$$

where C_A is the specific areal capacitance, C_m is the specific mass capacitance, I_d is the discharge current, t is the discharge time, ΔV is the operating potential during the discharge process, A is the active area of the sample, and m is the mass of the active material. The loading mass of the active materials is 2.1 mg cm^{-2} and 4.1 mg cm^{-2} for the $ZnCo_2O_4$ and the $ZnCo_2O_4/NiMoO_4$ samples, respectively. The active carbon (AC)//$ZnCo_2O_4/NiMoO_4$ asymmetric supercapacitor (ASC) was prepared to test the full cell performance by fabricating a 2032–coin cell. The ASC was fabricated by using the AC as the anode material, the $ZnCo_2O_4/NiMoO_4$ heterostructure sample as the cathode material, a cellulose paper as the separator and 6.0 M KOH as the electrolyte solution. The charge balance and the loading mass of the AC electrode were optimized according to the following Equation 2:

$$Q_+ = Q_- \Rightarrow \frac{m_+}{m_-} = \frac{C_- * \Delta V_-}{C_+ * \Delta V_+} \quad (2)$$

where C_+ and C_- are the specific capacitance of the cathode and anode electrodes, respectively, and ΔV_+ and ΔV_- are the operating potential windows of the cathode and anode electrodes, respectively. The AC anode was constructed by using the active carbon as the active material, poly(vinylidene difluoride) as the binder, and Ketjen black as the conductive material. This solution was coated onto a compressed Ni foam as the current collector. The energy density and power density of the ASC can be calculated according to the following Equation 3:

$$E(energy) = \frac{1}{2} C_m \Delta V^2 \text{ and } P(power) = \frac{E}{t} \quad (3)$$

where C_m is the specific overall capacitance, E is the calculated energy density, ΔV is the overall

operating potential window, and t is the discharge time.

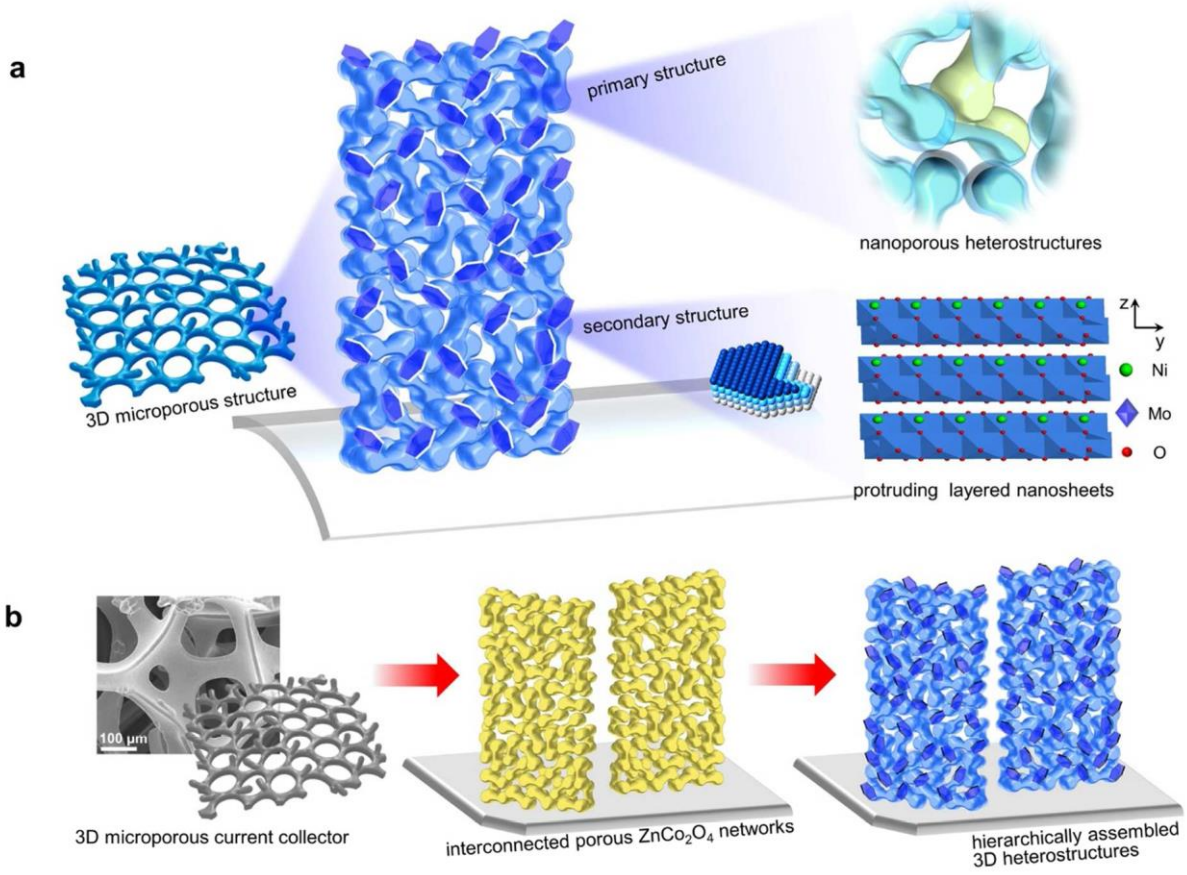

Figure 1. Illustrations of (a) the overall hierarchically assembled 3D $ZnCo_2O_4/NiMoO_4$ heterostructures and (b) the fabrication steps for 3D $ZnCo_2O_4/NiMoO_4$ heterostructures directly integrated on the 3D microporous conductive current collector through hierarchical bottom-up synthesis assembly.

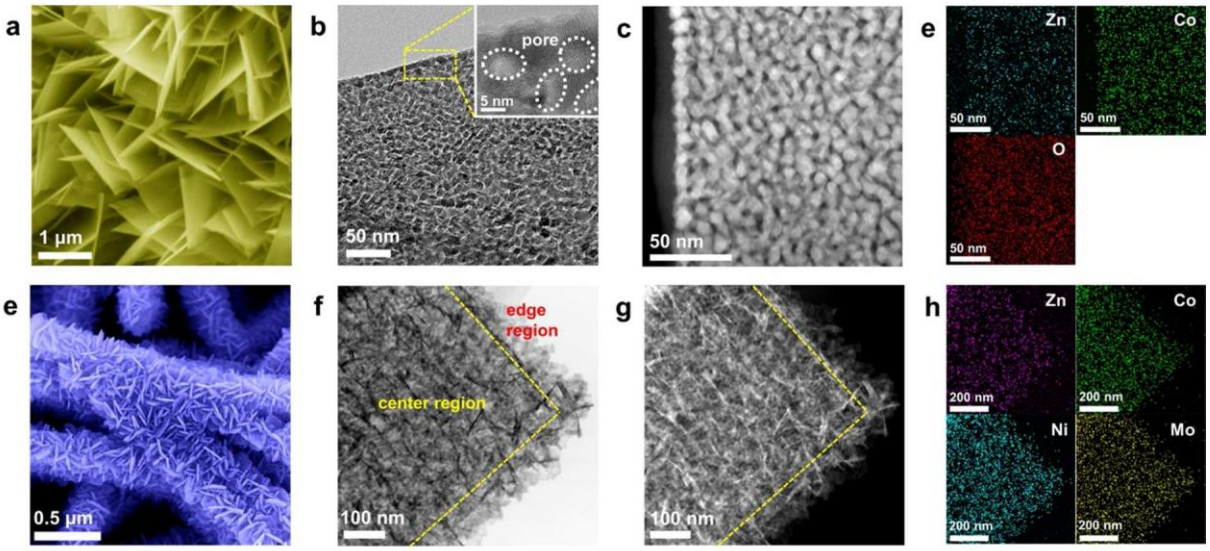

Figure 2. (a) SEM, (b) TEM, (c) HADDF-STEM, and (d) EDX mapping images of 3D nanoporous $ZnCo_2O_4$ serving as a back-bone structure. The inset image in Figure 2b indicates highly porous grains of $ZnCo_2O_4$. (e) SEM, (f) STEM, (g) HADDF-STEM, and (h) EDX mapping images of hierarchically assembled 3D $ZnCo_2O_4$/$NiMoO_4$ heterostructures.

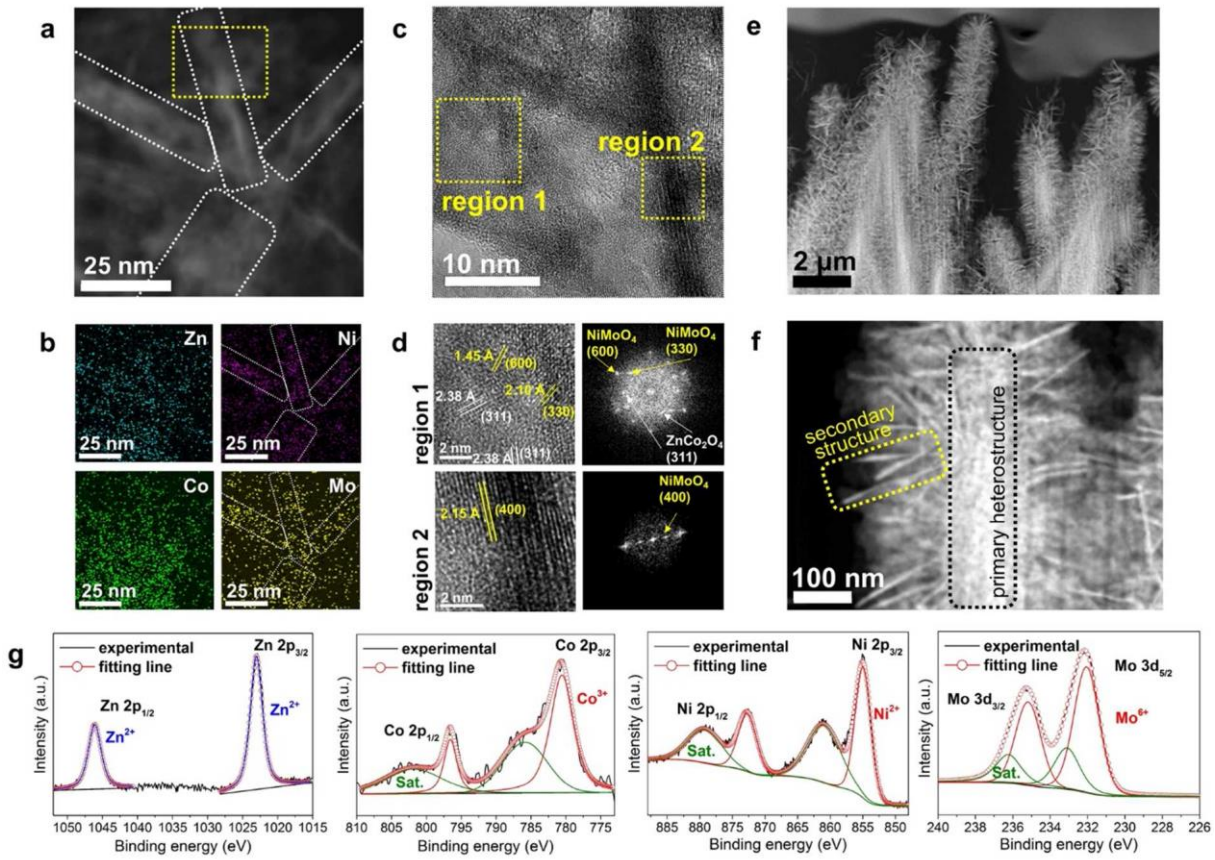

Figure 3. (a) A high-resolution HAADF-STEM and (b) EDX elemental mapping images of $ZnCo_2O_4/NiMoO_4$ heterostructures. (c) A high-resolution TEM image of $ZnCo_2O_4/NiMoO_4$ heterostructures taken from the region outlined by the yellow dotted rectangle in Figure 3a. (d) High-resolution TEM and FFT images of the region 1 indicate existence of primary heterostructures of the $NiMoO_4$ shell and the rigid $ZnCo_2O_4$ core. High-resolution TEM and FFT images of region 2 indicate existence of secondary layered $NiMoO_4$ nanosheets. (e) A low-resolution and (f) high-resolution cross sectional HAADF-STEM images of $ZnCo_2O_4/NiMoO_4$ heterostructures. (g) XPS Zn 2p, Co 2p, Ni 2p, and Mo 3d spectra of $ZnCo_2O_4/NiMoO_4$ heterostructures.

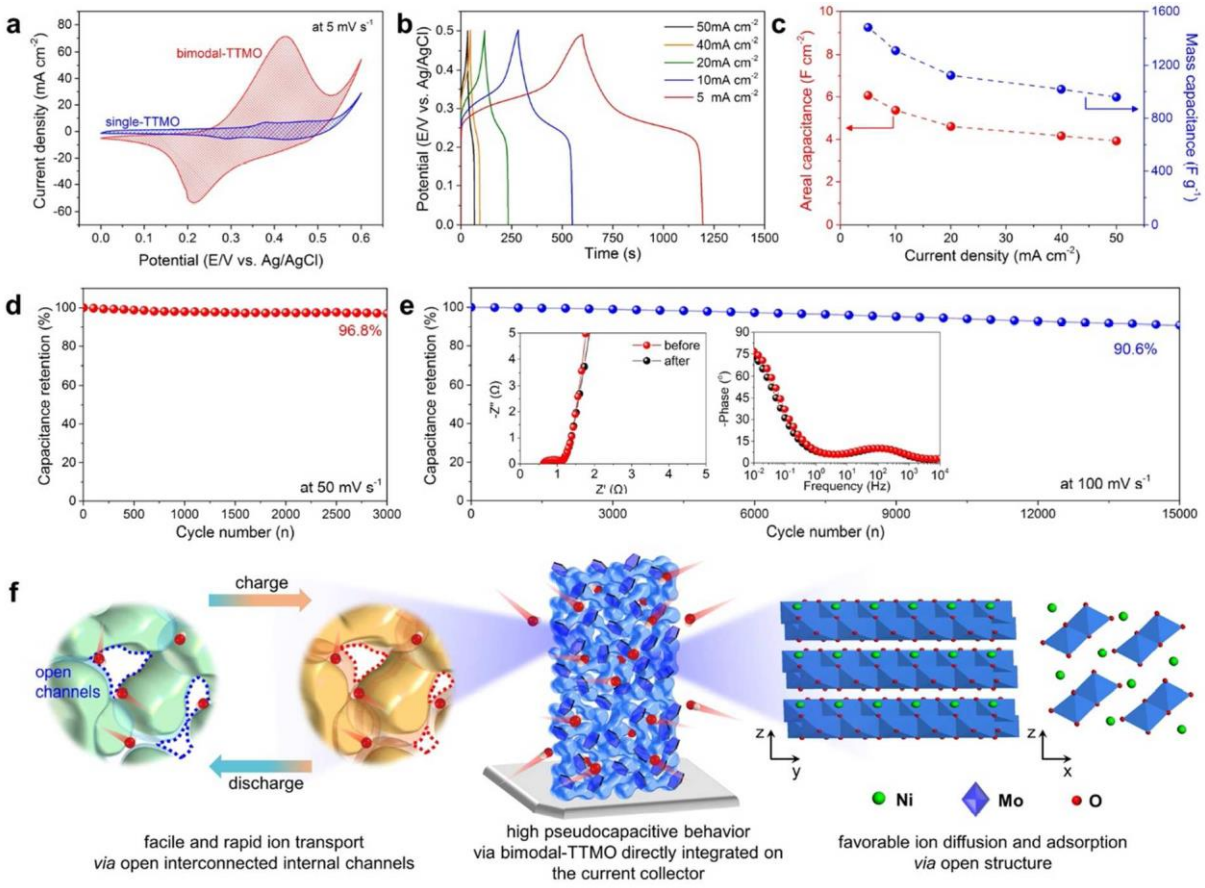

Figure 4. (a) CV curves of bimodal-TTMO and single-TTMO at a scan rate of 5 mV s^{-1}. (b) GCD curves of bimodal-TTMO at different current densities. (c) Specific capacitances of bimodal-TTMO at different current densities. (d) Cycle performance of bimodal-TTMO at a scan rate of 50 mV s^{-1} up to 3000 cycling charge/discharge tests. (e) Under harsh conditions, cycle performance of bimodal-TTMO at a scan rate of 100 mV s^{-1} up to 15000 cycling charge/discharge tests. The insets in Figure 4e indicate Nyquist plots and Bode plots of bimodal-TTMO before and after long-term cycling tests. (f) Illustration showing pseudo-capacitive behavior in hierarchically assembled 3D $ZnCo_2O_4/NiMoO_4$ heterostructures.

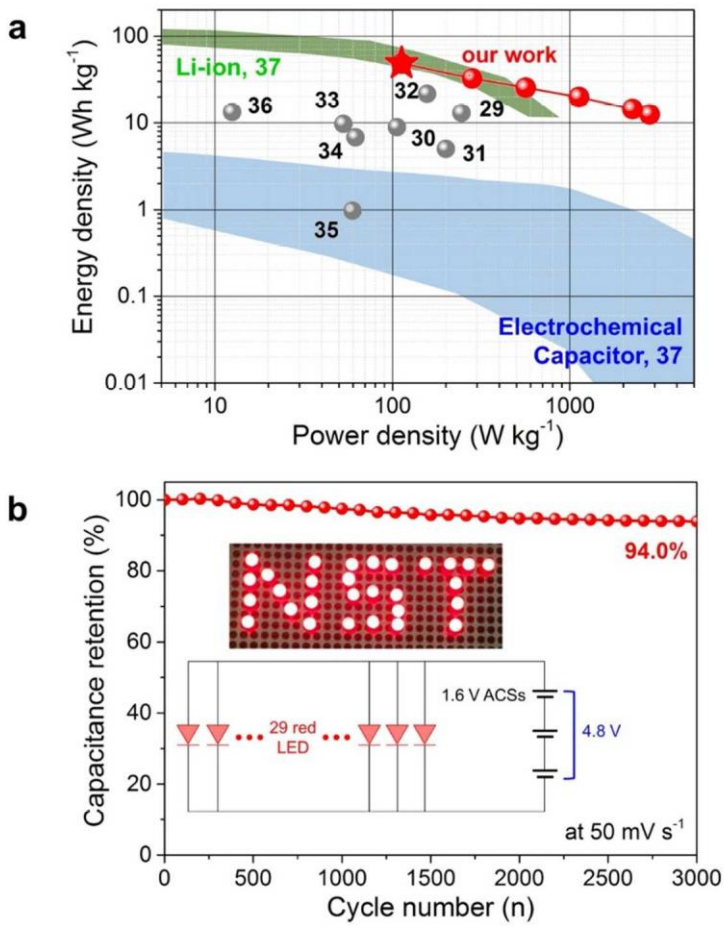

Figure 5. (a) Ragone plots of the AC//$ZnCo_2O_4$/$NiMoO_4$ ASC as well as other, recently reported, pseudo-capacitive ASCs. (b) Cycle performance of the AC//$ZnCo_2O_4$/$NiMoO_4$ ASC at a scan rate of 50 mV s^{-1} up to 3000 cycling charge/discharge tests. The inset in Figure 5b are photographs showing three ASCs in series that can light up 29 red LEDs.

ASSOCIATED CONTENT

Supporting Information. Additional structural and electrochemical analysis data in Figure S1-S10 and Table S1.

AUTHOR INFORMATION

Corresponding Author

*E-mail: shin@unist.ac.kr (H.S.S.) and junginn.sohn@eng.ox.ac.uk (J.I.S.)

Author Contributions

‡These authors contributed equally.

Notes

The authors declare no competing financial interest.

ACKNOWLEDGMENT

This research was supported by the Industrial Fundamental Technology Development Program (10052745, Development of the nano-sized (100 nm) manganese ceramic material for high voltage pseudo-capacitor) funded by the Ministry of Trade, Industry and Energy (MOTIE) of Korea, and the European Research Council under the European Union's Seventh Framework Programme (FP/2007-2013)/Grant Agreement no. 685758, Project '1D-NEON'. In addition, SMM would also like to thank The Royal Society for financial support.

REFERENCES

(1) Dresselhaus, M. S.; Thomas, I. L. Alternative Energy Technologies. *Nature* **2001,** *414,* 332–337.

(2) Miller, J.; Simon, P. Electrochemical Capacitors for Energy Management. *Science* **2008,** *321,* 651–652.

(3) Salanne, M.; Rotenberg, B.; Naoi, K.; Kaneko, K.; Taberna, P.-L.; Grey, C. P.; Dunn, B.; Simon, P. Efficient Storage Mechanisms for Building Better Supercapacitors. *Nat. Energy* **2016,** *1,* 16070.

(4) Peng, Y.-Y.; Akuzum, B.; Kurra, N.; Zhao, M.-Q.; Alhabeb, M.; Anasori, B.; Kumbur, E. C.; Alshareef, H.; Ger, M.-D.; Gogotsi, Y. All-MXene (2D Titanium Carbide) Solid-State Microsupercapacitors for On-Chip Energy Storage. *Energy Environ. Sci.* **2016,** *9,* 2847–2854.

(5) Simon, P.; Gogotsi, Y.; Dunn, B. Where Do Batteries End and Supercapacitors Begin?. *Science* **2014,** *343,* 1210–1211.

(6) Arico, A. S.; Bruce, P.; Scrosati, B.; Tarascon, J.-M.; Schalkwijk, W. Nanostructured Materials for Advanced Energy Conversion and Storage Devices. *Nat. Mater.* **2005,** *4,* 366–377.

(7) Wang, G.; Zhang, L.; Zhang, J. A Review of Electrode Materials for Electrochemical Supercapacitors. *Chem. Soc. Rev.* **2012,** *41,* 797–828.

(8) Li, X.; Jiang, L.; Zhou, C.; Liu, J.; Zeng, H. Integrating Large Specific Surface Area and High Conductivity in Hydrogenated $NiCo_2O_4$ Double-Shell Hollow Spheres to Improve Supercapacitors. *NPG Asia Mater.* **2015,** *7,* e165.

(9) Chen, H.; Hu, L.; Chen, M.; Yan, Y.; Wu, L. Nickel–Cobalt Layered Double Hydroxide Nanosheets for High-performance Supercapacitor Electrode Materials. *Adv. Funct. Mater.* **2014,** *24,* 934–942.

(10) Toupin, M.; Brousse, T.; Bélanger, D. Charge Storage Mechanism of MnO_2 Electrode Used in Aqueous Electrochemical Capacitor. *Chem. Mater.* **2004,** *16,* 3184–3190.

(11) Lee, Y.-W.; Kim, B.-S.; Hong, J.; Lee, J.; Pak, S.; Jang, H.-S.; Whang, D.; Cha, S.-N.; Sohn, J. I.; Kim, J. M. A Pseudo-Capacitive Chalcogenide-Based Electrode with Dense 1-Dimensional Nanoarrays for Enhanced Energy Density in Asymmetric Supercapacitors. *J. Mater. Chem. A* **2016,** *4,* 10084–10090.

(12) Mefford, T.; Hardin, W.; Dai, S.; Johnston, K.; Stevenson, K. Anion Charge Storage through Oxygen Intercalation in $LaMnO_3$ Perovskite Pseudocapacitor Electrodes. *Nat. Mater.* **2014,** *13,* 726–732.

(13) Chen, D.; Wang, Q.; Wang, R.; Shen, G. Ternary Oxide Nanostructured Materials for Supercapacitors: A Review. *J. Mater. Chem. A* **2015,** *3,* 10158–10173.

(14) Ren, X.; Guo, C.; Xu, L.; Li, T.; Hou, L.; Wei, Y. Facile Synthesis of Hierarchical Mesoporous Honeycomb-like NiO for Aqueous Asymmetric Supercapacitors. *ACS Appl. Mater. Interfaces* **2015,** *7,* 19930–19940.

(15) Qiu, Y.; Yang, S.; Deng, H.; Jin, L.; Li, W. A Novel Nanostructured Spinel $ZnCo_2O_4$ Electrode Material: Morphology Conserved Transformation from a Hexagonal Shaped Nanodisk Precursor and Application in Lithium Ion Batteries. *J. Mater. Chem.* **2010,** *20,* 4439–4444.

(16) Liu, B.; Zhang, J.; Wang, X.; Chen, G.; Chen, D.; Zhou, C.; Shen, G. Hierarchical Three-Dimensional $ZnCo_2O_4$ Nanowire Arrays/Carbon Cloth Anodes for a Novel

Class of High-Performance Flexible Lithium-Ion Batteries. *Nano Lett.* **2012,** *12,* 3005–3011.

(17) Zhang, D.; Zhang, Y.; Li, X.; Luo, Y.; Huang, H.; Wang, J.; Chu, P. K. Self-Assembly of Mesoporous ZnCo2O4 Nanomaterials: Density Functional Theory Calculation and Flexible All-Solid-State Energy Storage. *J. Mater. Chem. A* **2016,** *4,* 568–577.

(18) Yin, Z.; Zhang, S.; Chen, Y.; Gao, P.; Zhu, C.; Yang, P.; Qi, L. Hierarchical Nanosheet-Based $NiMoO_4$ Nanotubes: Synthesis and High Supercapacitor Performance. *J. Mater. Chem. A* **2015,** *3,* 739–745.

(19) Xiao, K.; Xia, L.; Liu, G.; Wang, S.; Ding, L.-X.; Wang, H. Honeycomb-like $NiMoO_4$ Ultrathin Nanosheet Arrays for High-Performance Electrochemical Energy Storage. *J. Mater. Chem. A* **2015,** *3,* 6128–6135.

(20) Gai, Y.; Shang, Y.; Gong, L.; Su, L.; Hao, L.; Dong, F.; Li, J. A Self-Template Synthesis of Porous $ZnCo_2O_4$ Microspheres for High-Performance Quasi-Solid-State Asymmetric Supercapacitors. *RSC Adv.* **2017,** *7,* 1038–1044.

(21) Peng, S.; Li, L.; Wu, H. B.; Madhavi, S.; Lou, X. W. Controlled Growth of $NiMoO_4$ Nanosheet and Nanorod Arrays on Various Conductive Substrates as Advanced Electrodes for Asymmetric Supercapacitors. *Adv. Energy Mater.* **2015,** *5,* 1401172.

(22) Gao, G.; Wu, H. B.; Dong, B.; Ding, S.; Lou, X. W. Growth of Ultrathin $ZnCo_2O_4$ Nanosheets on Reduced Graphene Oxide with Enhanced Lithium Storage Properties. *Adv. Sci.* **2015,** *2,* 1400014.

(23) Huang, L.; Zhang, W.; Xiang, J.; Xu, H.; Li, G.; Huang, Y. Hierarchical Core-Shell $NiCo_2O_4$@$NiMoO_4$ Nanowires Grown on Carbon Cloth as Integrated Electrode for High-Performance Supercapacitors. *Sci. Rep.* **2016,** *6,* 31465.

(24) Qiu, K.; Lu, Y.; Zhang, D.; Cheng, J.; Yan, H.; Xu, J.; Liu, X.; Kim, J.-K.; Luo, Y. Mesoporous, hierarchical core/shell structured $ZnCo_2O_4/MnO_2$ nanocone forests for high-performance supercapacitors. *Nano Energy* **2015,** *11,* 687–696.

(25) Hong, J.; Lee, Y.-W.; Hou, B.; Ko, W.; Lee, J.; Pak, S.; Hong, J.-P.; Morris, S.; Cha, S.-N.; Sohn, J. I.; Kim, J. M. Solubility-Dependent $NiMoO_4$ Nanoarchitectures: Direct Correlation between Rationally Designed Structure and Electrochemical Pseudokinetics. *ACS Appl. Mater. Interfaces* **2016,** *8,* 35227–35234.

(26) Wang, H.; Yi, H.; Zhu, C.; Wang, X.; Fan, H. J. Functionalized Highly Porous Graphitic Carbon Fibers for High-Rate Supercapacitive Electrodes. *Nano Energy* **2015,** *13,* 658–669.

(27) Yuan, L.; Lu, X.-H.; Xiao, X.; Zhai, T.; Dai, J.; Zhang, F.; Hu, B.; Wang, X.; Gong, L.; Chen, J.; Hu, C.; Tong, Y.; Zhou, J.; Wang, Z. L. Flexible Solid-State Supercapacitors Based on Carbon Nanoparticles/MnO_2 Nanorods Hybrid Structure. *ACS Nano* **2012,** *6,* 656–661.

(28) Masikhwa, T.; Madito, M.; Momodu, D.; Dangbegnon, J.; Guellati, O.; Harat, A.; Guerioune, M.; Barzegar, F.; Manyala, N. High Performance Asymmetric Supercapacitor Based on CoAl-LDH/GF and Activated Carbon from Expanded Graphite. *RSC Adv.* **2016,** *6,* 46723–46732.

(29) Cai, D.; Wang, D.; Liu, B.; Wang, Y.; Liu, Y.; Wang, L.; Li, H.; Huang, H.; Li, Q.; Wang, T. Comparison of the Electrochemical Performance of $NiMoO_4$ Nanorods and Hierarchical Nanospheres for Supercapacitor Applications. *ACS Appl. Mater. Interfaces* **2013,** *5,* 12905–12910.

(30) Cheng, Y.; Lu, S.; Zhang, H.; Varanasi, C.; Liu, J. Synergistic Effects from Graphene and Carbon Nanotubes Enable Flexible and Robust Electrodes for High-Performance Supercapacitors. *Nano Lett.* **2012,** *12,* 4206–4211.

(31) Cai, W.; Lai, T.; Dai, W.; Ye, J. A Facile Approach to Fabricate Flexible All-Solid-State Supercapacitors Based on $MnFe_2O_4$/Graphene Hybrids. *J. Power Sources* **2014,** *255,* 170–178.

(32) Cheng, D.; Yang, Y.; Xie, J.; Fang, C.; Zhang, G.; Xiong, J. Hierarchical $NiCo_2O_4$@$NiMoO_4$ Core-Shell Hybrid Nanowire/Nanosheet Arrays for High-Performance Pseudocapacitors. *J. Mater. Chem. A* **2015,** *3,* 14348–14357.

(33) Zou, B.-X.; Liang, Y.; Liu, X.-X.; Diamond, D.; Lau, K.-T. Electrodeposition and Pseudocapacitive Properties of Tungsten Oxide/Polyaniline Composite. *J. Power Sources* **2011,** *196,* 4842–4848.

(34) He, Y.; Chen, W.; Li, X.; Zhang, Z.; Fu, J.; Zhao, C.; Xie, E. Freestanding Three-Dimensional Graphene/MnO_2 Composite Networks as Ultralight and Flexible Supercapacitor Electrodes. *ACS Nano* **2013,** *7,* 174–182.

(35) Ramasamy, K.; Gupta, R.; Palchoudhury, S.; Ivanov, S.; Gupta, A. Layer-Structured Copper Antimony Chalcogenides ($CuSbSe_xS_{2-x}$): Stable Electrode Materials for Supercapacitors. *Chem. Mater.* **2015,** *27,* 379–386.

(36) Foo, C. Y.; Sumboja, A.; Tan, D. J. H.; Wang, J.; Lee, P. S. Flexible and Highly Scalable V_2O_5-rGO Electrodes in an Organic Electrolyte for Supercapacitor Devices. *Adv. Energy Mater.* **2014,** *4,* 1400236.

(37) Simon, P.; Gogotsi, Y. Materials for Electrochemical Capacitors. *Nat. Mater.* **2008,** *7,* 845–854.

Table of Contents